Multiphase inclusions associated with residual carbonate in a transition zone diamond from Juina (Brazil)

Agrosì Giovanna [a] 🖂, Tempesta Gioacchino [a], Mele Daniela [a], Caggiani Maria Cristina [b], Mangone Annarosa [b], Della Ventura Giancarlo [c, d], Cestelli-Guidi Mariangela [d], Allegretta Ignazio [e], Mark T. Hutchison [f] 🖂, Nimis Paolo [g], Nestola Fabrizio [g]

⊞ Show more

Highlights

- Non-destructive analyses of multiphase inclusions in a diamond from Juina.

- Evidence of diamond growth in a carbonate-rich environment at Transition-Zone depths.

- First occurrence of maohokite and huntite in diamond.

- Evidence of partial diamond resorption by oxidizing melt.

- Syngenetic magnetite and hematite by oxidation of ferropericlase–magnesiowüstite.

ABSTRACT

Super-deep diamonds and their mineral inclusions preserve very precious information about Earth's deep mantle. In this study, we examined multiphase inclusions entrapped within a diamond from the Rio Vinte e um de Abril, São Luiz area (Juina, Brazil), using a combination of non-destructive methods. Micro-Computed X-ray Tomography (μ-CXRT) was used to investigate the size, shape, distribution and X-Ray absorption of inclusions and mapping by micro X-ray Fluorescence (μ-XRF), μ-Raman Spectroscopy and micro-Fourier Transform Infrared Spectroscopy (μ-FTIR) were used to determine the chemical and mineralogical composition of the inclusions. Four large inclusions enclosed in the N-rich diamond core consist of dominant ferropericlase–magnesiowüstite and locally exsolved magnesioferrite. FTIR maps, obtained integrating the band at 1430 cm^{-1}, show also the presence of carbonates. A fifth large inclusion (ca 100 μm) was remarkable because it showed a very unusual flask shape, resembling a fluid/melt inclusion. Based on μCXRT tomography and μ-Raman mapping, the flask-shaped inclusion is polyphase and consists of magnetite and hematite partly replacing a magnesiowüstite core and small-volume of gas/vacuum. μ-Raman spectra on the same inclusion revealed local features that are ascribed to post-spinel polymorphs, such as maohokite or xieite, which are stable at P $\geq$ 18 GPa, and to huntite, a carbonate with formula CaMg$_3$(CO$_3$)$_4$. This represents the first finding of maohokite and huntite in diamond. We interpret the composition of the inclusions as evidence of formation of ferropericlase–magnesiowüstite and diamond in a carbonate-rich environment at depths corresponding at least to the Transition Zone, followed by oxidation of ferropericlase–magnesiowüstite by reaction with relatively large-volume entrapped melt during diamond ascent.

Keywords

diamond; Transition Zone; syngenetic inclusions; post-spinel polymorphs; Fe^{3+}-rich iron oxides

INTRODUCTION

Diamonds and their inclusions preserve valuable information about physico-chemical conditions in the deep mantle, thus providing geochemical, petrogenetic and geophysical constraints on inaccessible portions of the Earth. In particular, inclusions in superdeep diamonds, originating from the sub-lithospheric mantle (depths greater than ca. 200 km), may provide indications of diamond formation depths and can shed light on the composition and redox conditions of the Lower Mantle (e.g. Palot et al., 2016, Smith et al., 2016; Nestola et al., 2018, Kiseeva et al., 2018). The inclusions trapped within superdeep diamonds may re-equilibrate during ascent toward the surface, converting to lower-pressure minerals and sometimes yielding composite assemblages (Smith et al., 2018). Multiphase inclusions offer an important opportunity to explore the complex processes occurring in the mantle and their analysis may significantly contribute to our understanding of the origin of superdeep diamonds.

In this work, we studied inclusions in a brownish diamond crystal (JUc4), taken from the Rio Vinte e um de abril (WGS84 Zone 21S 261000; 8708000) which, like the better-known Rio São Luiz, is a small tributary of the Rio Aripuanã west of the town of Juina (Mato Grosso, Brazil). The diamonds coming from Juina are commonly considered superdeep diamonds due to the mineralogical nature of their inclusions (Harte et al., 1999). Our specimen was previously studied by Agrosì et al. (2017a) and Nimis et al. (2019). In these previous papers it was found that diamond JUc4 has nitrogen occurring in clusters of three atoms and a vacancy (Type IaB), has a N-enriched core, is plastically deformed (Agrosì et al., 2017a), and contains several syngenetic, relatively Fe-rich ferropericlase–magnesiowüstite inclusions in its N-rich core (Nimis et al., 2019). Compared with other similar diamonds from Juina, this sample is remarkable because it encases an atypical inclusion, which shows a very unusual flask shape resembling a large (ca 100 μm) fluid/melt inclusion. This inclusion merited further detailed examination to understand its nature and genesis. For this work, we chose to use a combination of *in situ* non-destructive techniques to guarantee the integrity of the sample and the reproducibility of the analyses and to avoid loss of precious material for future investigation (Agrosì et al., 2017b; Nestola et al., 2018). The multi-analytical approach consisted of micro-Computed X-ray Tomography (μ-CXRT) to investigate the size, shape, distribution and X-Ray absorption of inclusions, micro X-ray Fluorescence (μ-XRF) to determine the chemical composition of the inclusions; μ-Raman Spectroscopy and micro-Fourier Transform Infrared Spectroscopy (μ-FTIR) to examine their mineralogical composition. On one inclusion located a few μm from the surface of the diamond host, we used a minimally destructive technique (micro-Laser Induced Breakdown Spectroscopy, μ-LIBS; Tempesta et al., 2011) to unambiguously characterize its chemical composition.

The results obtained in this work indicate formation of the ferropericlase–magnesiowüstite-bearing diamond in a carbonate-rich environment at depths corresponding at least to the mantle Transition Zone.

METHODS

μ-CXRT

The instrument utilized was a Bruker Skyscan 1172 high-resolution μX-Ct scanner equipped with a W tube. A 49 kV X-ray source was used with a current of 200 μA. A total of 1332 absorption radiographs were acquired over a 360° rotation with an angular step of 0.4°. Beam hardening was reduced by the presence of a 0.5 mm Al-filter between source and detector. The nominal spatial resolution for the resulting model was about 1 μm. The raw data were reconstructed into two-dimensional slice images using Bruker's NRecon software. Corrections for the beam-hardening effect and ring artefacts were also applied during the reconstruction process. μCXRT datasets were analyzed using Bruker's CTAn software.

μ-XRF

Chemical analyses were obtained by means of a conventional source using an M4 Tornado μXRF (Bruker Nano GmbH, Berlin) equipped with a Rh tube with policapillary optics (50 kV, 600 μA, 30 W) and having a spot size of 25 μm. Two XFlash® silicon drift detectors with active areas of 30 mm² were used. The resolution was lower than 140 eV for both detectors. For elemental maps, one spectrum was acquired every 10 μm with both detectors, with acquisition time set at 10 ms per pixel. Elemental analyses on inclusions within the diamond were performed with only one detector in order to exclude diffraction peaks which can overlap heavy metal K-lines. A live time of 60 s was used. All analyses were performed under vacuum (20 mbar) to avoid Ar absorption and to facilitate the detect of light elements. Spectral quantification was performed in standardless mode using M4 Tornado software. NIST SRM 611 and NIST SRM 613 glass standards were analyzed in order to periodically test the performance of the instrument.

μ-Raman

Raman micro-spectroscopy analyses were carried out using a Horiba HR Evolution spectrometer, equipped with an Ar⁺ laser (488 and 514 nm lines) and with a He-Ne 633 nm laser. The bench is coupled with an Olympus microscope providing a long working distance x50 objective (N.A.= 0.50) used to avoid contact with the relatively large sample. Several tests were carried out with different excitation wavelengths, gratings and operational parameters in order to optimize the quality of the results. The

633 nm laser was used to analyse the iron-rich inclusions. The spectral resolution achieved with this laser coupled with a 1800 grooves/mm grating is ~ 1 cm^{-1}. Raman mapping and linear profiles were acquired with a grid of 8x11 and 9x10 spots at 5 μm step for the images, and 20 spots at 2 μm step for the linear profiles. The analyses were carried out using a laser power suitable to avoid the laser-induced oxidation of bivalent iron. Preliminary tests were conducted on the inclusions with a laser power of 0.03 mW lower than that recommended by de Faria et al. (1997) (0.7 mW) and by Antic et al. (2010) (0.1 mW). No damage to the sample or changes in the spectral features (position, relative intensity and peak shape) were observed.
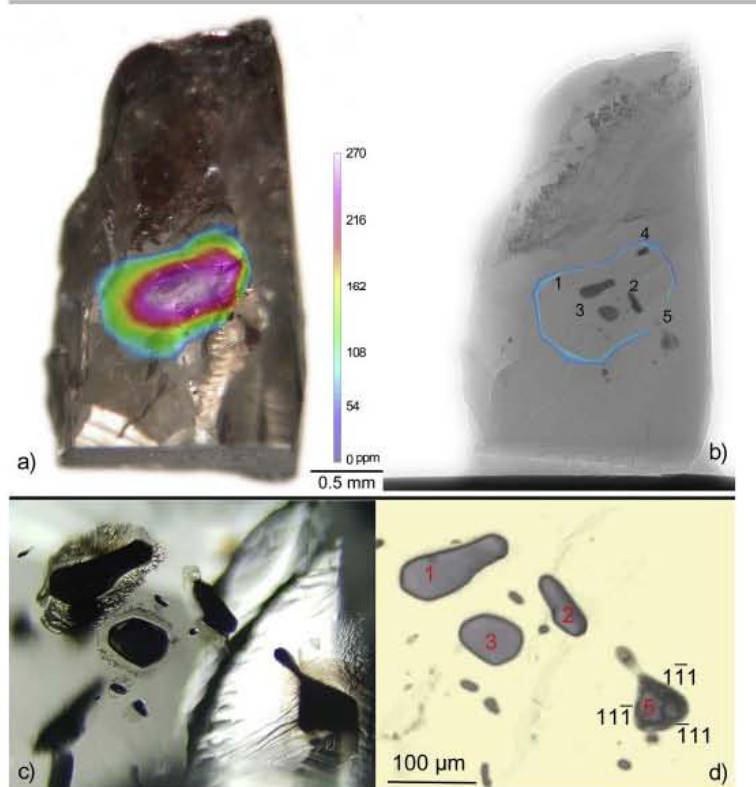
μ-FTIR

FTIR images were recorded in transmission mode using CaF_2 transparent windows with a Vertex 70V FTIR spectrometer combined with a Hyperion 3000 FTIR microscope (Bruker, Germany) and 64x64 focal plane array detector. A 15X cassegrain objective and a 15X condenser were used, giving a field of view of 170x170 μm per single image with a detector pixel size of 2.6x2.6 μm (Della Ventura et al., 2014). Due to the large sample size, a mosaic consisting of several FTIR images covering the whole area of interest was collected; the single frames were composed into one image, the largest of which (Fig. 7, panel c) was 510x850 μm (3x5 mosaic size). Due to the very large image size, binning was performed averaging 2x2 or 4x4 adjacent pixels to allow a reduction of CPU usage when performing analysis on the dataset. Spectra were acquired in the range 850-4000 cm^{-1} at a spectral resolution of 4 cm^{-1} with 128 accumulated scans.

μ-LIBS

The Laser Induced Breakdown Spectroscopy (LIBS) system coupled with a petrographic optical microscope (objective lens: 10X NA 0.25 WD 14.75 mm), allowed the analyses of small inclusions very close to the surface (ca 5 μm). A Nd:YAG Laser source generates two beams in collinear geometry both at 1064 nm for the acquisition of double-pulse (DP) spectra. The plasma emission was collected using an optical fibre Avantes spectrometer with a spectral range 190-400 nm and a resolution of 0.2 nm. The beam size is ca 7 μm. The analyses performed in this study consisted of 5 consecutive shots on the same inclusion using 75mJ of laser power. Quantitative chemical data were obtained using the Calibration Free CFLIBS method (Ciucci et al., 1999).

RESULTS

Diamond JUc4 has an irregular morphology that appears partially flattened along the (111) plane. Optical observations revealed anomalous birefringence and the presence of five large inclusions (labelled 1 to 5) and several tiny optically opaque inclusions. Most of these inclusions have a polygonal shape, but one of the large inclusions (inclusion 5) shows an unusual rounded flask shape (Fig. 1). Small decompression cracks partially filled with dark material are visible around the large polygonal inclusions, but not around the flask-shaped inclusion 5. However, there is no evidence of open or annealed cracks connecting the inclusions with the surface of the diamond, suggesting that the inclusions did not exchange with the external ambient and their chemical integrity was not compromised (Fig. 1a and 1b). The comparison between the detailed spatial distribution of the inclusions and the N zoning in the diamond (Agrosì et al., 2017a) shows that the inclusions 1, 2, 3 and 4 are located within the inner, N-rich core of the diamond, whereas inclusion 5 is located in a more external diamond growth zone, near a sudden break of the zoning of N and H point defects (Fig. 1b).
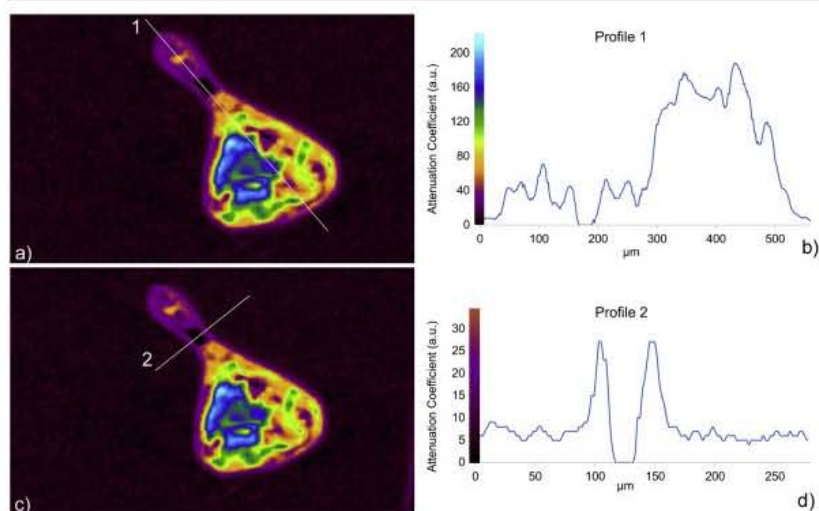
Figure 1. diamond JUc 4. a) Optical image of the sample with superimposed FTIR map of N point defect concentration. The zone with the highest N concentration marks the core of the diamond (modified after Agrosi et al., 2017a). The color-coding shows the ppm of nitrogen content. b) μ-CXRT image with the boundary corresponding to the N-rich core as shown in a). Note that inclusions 1, 2, 3 and 4 are located within the early N-rich core, whereas inclusion 5 lies in a later diamond growth zone. c) Enlarged optical image of the core. d) μ-CXRT image (volume rendering) of the same area in c). Note that the inclusion number 5 is multiphase and exhibits a flask shape. The body of flask shows a triangular shape in 2D, with surfaces corresponding to diamond octahedral faces (Miller indices annotated).

More detailed indications on the morphology, size and distribution of the inclusions were obtained by thresholding the grey value histogram of the reconstructed 3D images obtained by μ-CXRT (see video 1 in repository file and Fig. 1d). The five large inclusions are 100 to 300 μm in diameter and their shape generally appears to be flattened along the (111) plane. Inclusions 1, 2, 3 and 4 exhibit complex polygonal shapes. These inclusions exhibit a similar and uniform grey value, indicating their mono-mineralic nature and similar degree of X-ray absorption. In contrast, the flask-shaped inclusion 5 is clearly multiphase, as indicated by the presence of zones with high, moderate and very low X-ray absorption values (see video 1 in repository file and Fig. 2). In particular, at the bottleneck, X-ray absorption drops below the value of diamond, suggesting the presence of a void or gas representing about 3% of the total volume of the inclusion. Detailed analysis of μ-CXRT images confirms the absence of cracks surrounding this inclusion, excluding any post-entrapment contamination (Fig. 1d and Fig. 2).
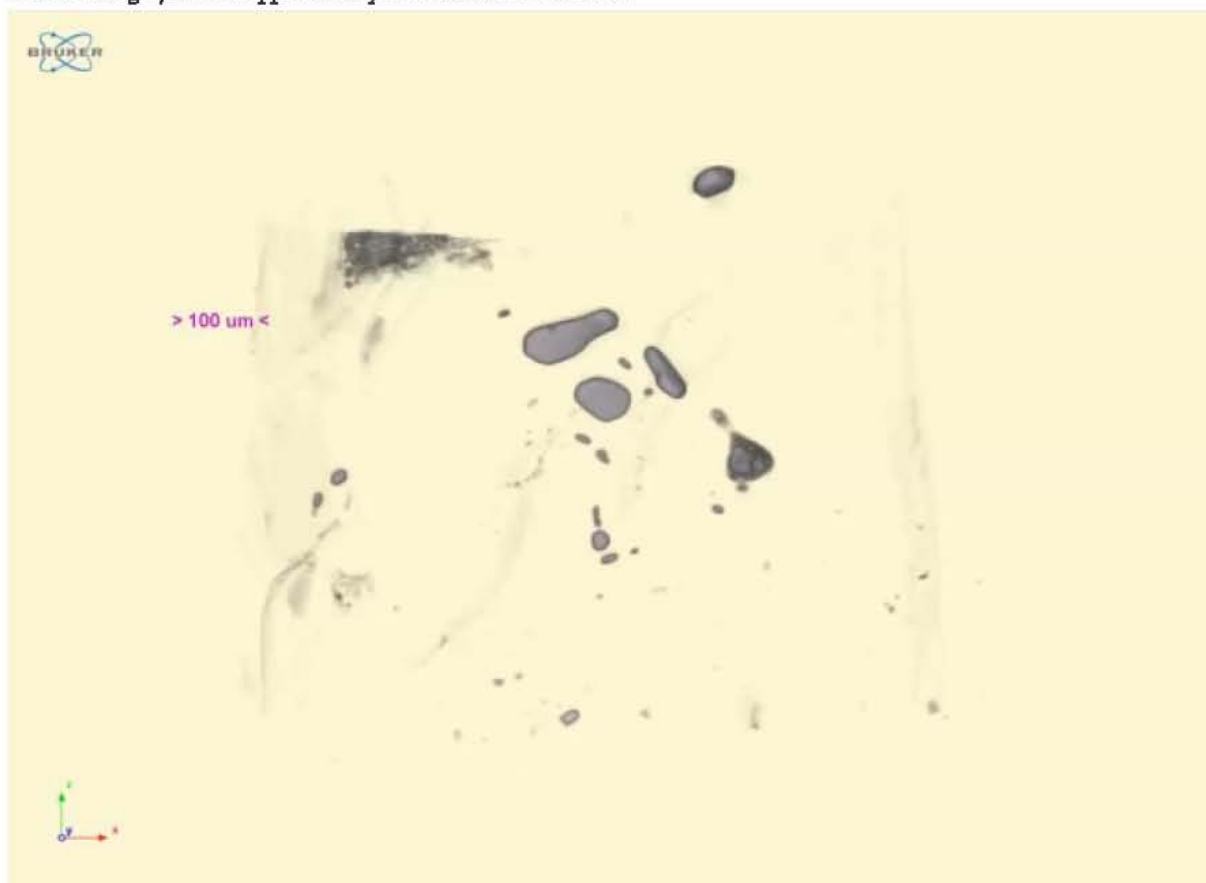
Figure 2. a) µ-CXRT slice of reconstructed 3D-image taken across inclusion 5 with longitudinal x-ray absorption profile 1 (white line). b) X-ray absorption profile 1. The attenuation coefficients (arbitrary units) with the corresponding color-coding used in a) are reported on the Y axis. The distance (µm) is reported on axis X. c) µ-CXRT slice of reconstructed 3D-image taken crossing the bottleneck of inclusion 5 with x-ray absorption profile 2 (white line). d). X-ray absorption profile 2. The attenuation coefficients (arbitrary units) with the corresponding color-coding used in c) are reported on axis Y. The distance (µm) is reported on axis X.

The following is/are the supplementary data related to this article:

Video 1. 3D animated version of the diamond crystal (JUc4) by µ-CXRT tomography showing the five large inclusions.

Previous in situ X-ray diffraction analyses of inclusions 2, 3, 4 and 5 gave crystallographic parameters corresponding to relatively Fe-rich (X_{Fe} = 0.43 to 0.64) members of the periclase–wüstite series (Nimis et al., 2019). These X_{Fe} values were regarded as minimum values, considering the possibility that the inclusions can be under non-null residual pressure. The μ-XRF maps confirm that all inclusions mainly consist of iron-rich phases (Fig. 3a). However, this technique does not permit determination of the abundance of Mg, as its characteristic radiation energy is fully absorbed by diamond. More quantitative chemical data were obtained by μ-LIBS, an innovative although partly destructive technique. Inclusion number 4 was chosen for this analysis, as it occurred only ca 5 μm from the diamond surface and, thus, required only minimal loss of material. Quantitative analysis of the LIBS spectra (Fig. 3b) with the CFLIBS method indicates that the inclusion is a magnesiowüstite with a chemical formula $(Fe_{0.56}Mg_{0.44})O$. This composition is consistent with the minimum X_{Fe} of 0.43 obtained by Nimis et al. (2019) for the same inclusion and confirms that the inclusion was under non-null residual pressure.
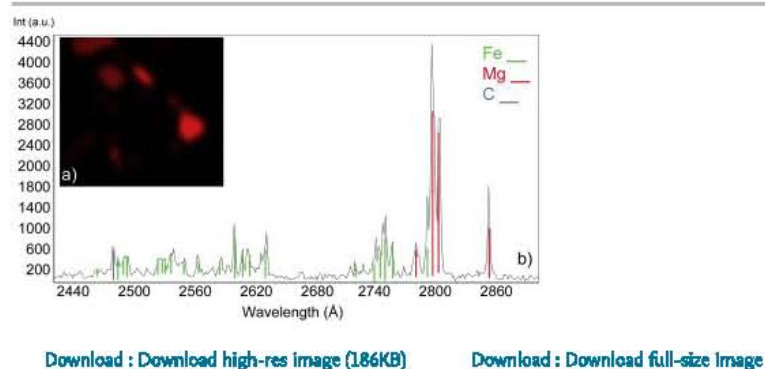
Figure 3. Chemical composition of inclusions. a) Non-destructive chemical analyses, performed by μXRF, showing that all the inclusions consist mainly of Fe. Mg is not detectable with this technique. b) Minimally destructive chemical analysis by LIBS, carried out on an inclusion very near (ca 5 μm) to the diamond surface showing emission lines of Fe and Mg.

Several μ-Raman spectra were acquired on inclusions 1, 2 and 3. All the acquired spectra exhibit only a single, relatively sharp peak at 690 cm^{-1} (see the representative spectrum shown in Fig. 4). Considering that ferropericlase and magnesiowüstite are Raman-inactive, the peak can be assigned to a nanostructured spinel-like mineral belonging to the ferrite group (D'Ippolito et al., 2015), which commonly forms exsolutions in ferropericlase–magnesiowüstite inclusions during the ascent of the diamond to accommodate excess Fe^{3+} (e.g., McCammon et al., 1997).
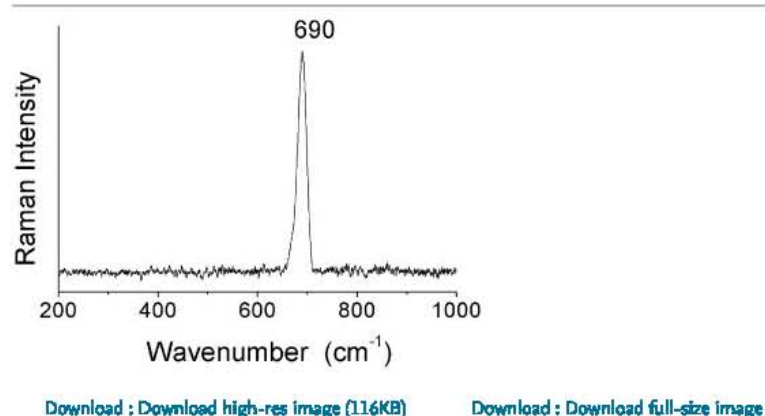
Figure 4. Raman spectrum acquired on ferropericlase/magnesiowüstite inclusion 1. This spectrum is representative of many analogous spectra acquired on the 1, 2 and 3 inclusions. The broad peak at 690 cm^{-1} corresponds to a spinel belonging to the ferrite group.

Given its unusual features, the flask-shaped inclusion 5 was investigated in greater detail. The μ-CXRT tomography (see video 2 with 3D reconstruction in repository file) shows that the inclusion mainly consists of a high-density inner portion (dark grey in Fig. 5b and turquoise in video2) surrounded by a material with lower absorbance (lighter grey in Fig. 5b and red in video 2). The

inner high-density material appears to be partially dismembered and shows abundant inlets infilled by the surrounding material. Figure 6a displays a representative Raman spectrum taken on this multiphase inclusion. The red peaks (229, 249, 296, 414, 500, 615 cm^{-1}) are assigned to hematite. The blue peaks (304, 666 cm^{-1}) gave a best match with magnetite (RRUFF ID: R080025), although peaks between 663 and 706 cm^{-1} could again more generally be assigned to spinels belonging to the ferrite group, such as magnetite or magnesioferrite (D'Ippolito et al., 2015). Detailed μ-Raman mapping was carried out near the bottleneck portion of the inclusion by integrating the characteristic band at 414 cm^{-1} of hematite (Fig. 5c) and at 666 cm^{-1} of magnetite (Fig. 5d). Raman analysis of the more internal, dark μ-CXRT area gave a flat pattern. μ-Raman mapping shows a distribution of hematite (red in Fig. 5c) and magnetite (blue in Fig. 5d) that corresponds to the low-density material with moderate X-ray absorption revealed by μ-CXRT (lighter grey in the Fig. 5b and red in the video 2). The inner, Raman-inactive, high-density zones (dark grey in Fig. 5b and turquoise in video 2) most likely correspond to the magnesiowüstite that was previously found by single-crystal X-ray diffraction (Nimis et al., 2019) (Fig. 7).

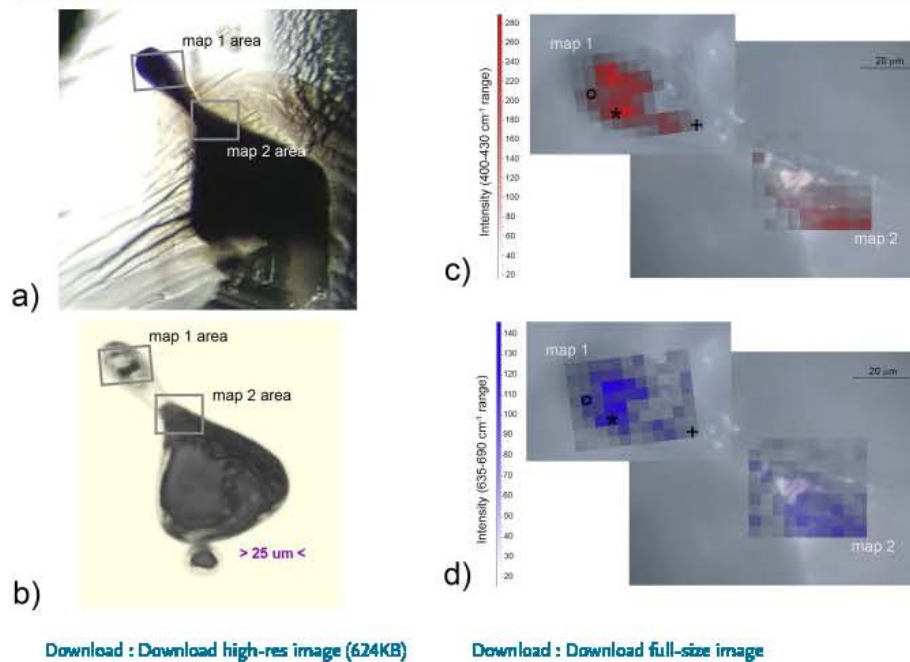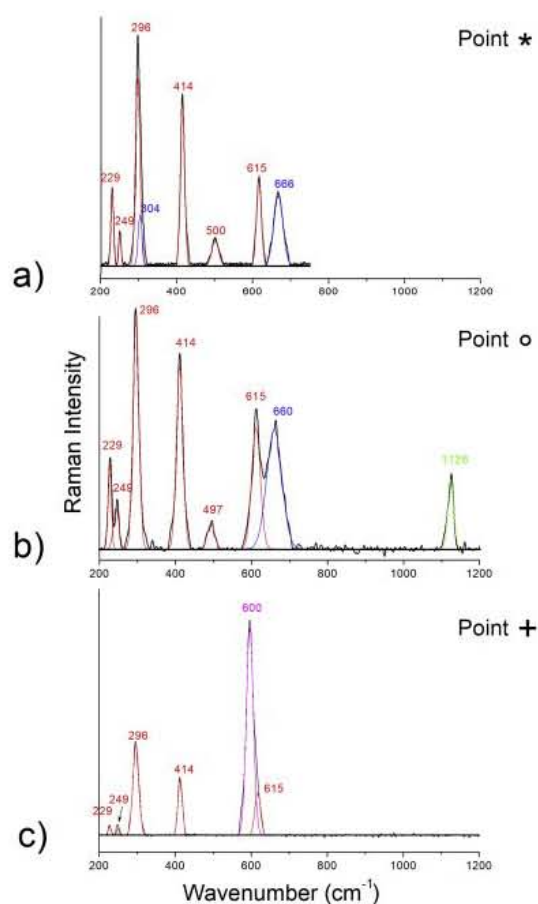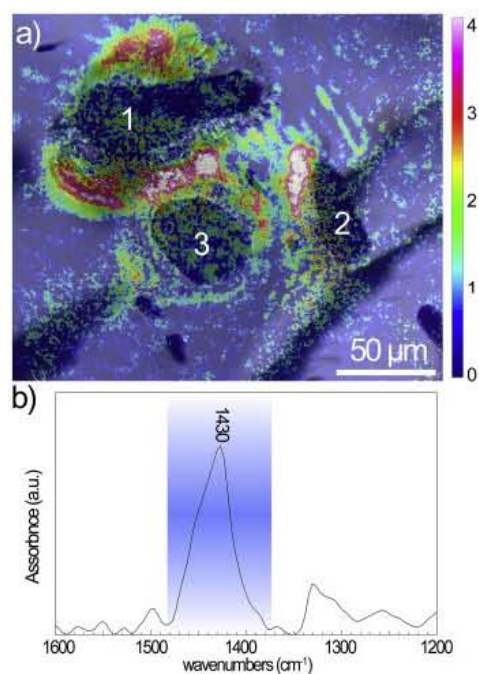Download : Download high-res image (624KB)   Download : Download full-size image

Figure 5. a) Optical micrograph of inclusion 5 showing the mapped areas. b) the corresponding μ-CXRT reconstruction. c) and d) μ-Raman maps acquired in the areas defined in (a and b), the intensity scales were maximized for each phase, each pixel is 5x5 μm: c) intensity distribution of the 414 cm^{-1} band assigned to hematite, d) intensity distribution of the 665 cm^{-1} band assigned to the ferrite-group spinels (magnetite/magnesioferrite). The o ∗ + symbols indicate the position of the corresponding spectra shown in Fig. 6.

Figure 6. Raman spectra selected from the mapping carried out on the inclusion 5 (at positions indicated in Fig. 5 by o * + symbols). Peaks assigned to different phases are marked by different colors. a) Raman spectrum collected at spot marked with * consists of the superposition of spectra of hematite (red) and spinel belonging to "ferrite group" (blue). b) spot marked with o where red corresponds to hematite, blue corresponds to magnetite/magnesioferrite and green corresponds to carbonates. c) analysis at the spot marked with + where red corresponds to hematite, blue corresponds to magnetite and the strong band pink corresponds to post-spinel polymorph.

Figure 7. High-resolution FTIR-FPA taken across the inclusion-rich area of diamond JUc4. a) intensity distribution (integration range 1370–1470 cm^{-1}) superimposed on the optical image of the corresponding diamond areas with the inclusions 1, 2 and 3 (see Fig. 1c). The color-coding shows the intensity of the respective band: blue stands for the lowest values, red and white for the highest values. b) FTIR spectrum with the band at 1430 cm^{-1} corresponding to the asymmetric stretching mode v_3 of the carbonate ion.

The following is/are the supplementary data related to this article:

Video 2. Movie animation of 3D rendering of the flask-shaped inclusion 5. Turquoise and red colours represent the high-density inner portion and the surrounded low-density material, respectively.

Additional Raman peaks were resolved in the spectra acquired near the rim of inclusion 5 (at points o and + in Fig. 5c, d). Their interpretations are challenging as they are based on single Raman lines. Nevertheless, we found very good matches with spectra for reasonable mineral phases. The strong band at ~600 cm^{-1} (Fig. 6c) can be assigned to a high-pressure orthorhombic polymorph of spinel, such as maohokite or xieite. In particular, maohokite ($MgFe_2O_4$) has its main Raman peak at about 602 cm^{-1} (Chen et al., 2019) and xieite ($FeCr_2O_4$) has its main Raman peak at 605 cm^{-1} (Chen et al., 2003, 2008). The prominent peak at 1126 cm^{-1} (Fig. 6b) can instead be ascribed to huntite, a carbonate with formula $CaMg_3(CO_3)_4$ (RRUFF ID R040126).

The presence of carbonates in diamond JUc4 are further supported by FTIR spectra, which show a well-resolved band at 1430 cm^{-1} (Fig. 7b), corresponding to the asymmetric stretching mode ν_3 of the carbonate ion (Pal'yanov et al. (2013). The intensity distribution of this band, observable in a FTIR map superimposed on the optical image of the corresponding diamond areas (Fig. 7a), reveals a higher carbonate concentration around inclusions 1, 2 and 3 in the regions corresponding to the optically visible "halo" and the small decompression cracks. Conversely, the FTIR signal corresponding to carbonates, is very low around the inclusion number 5, where no halo or cracks were optically observed. This finding suggests a presence of residual carbonates preferentially in the radial decompression cracks observed around the inclusions 1, 2 and 3 (see Fig. 1c). Nevertheless, the lower intensity of band at 1430 cm^{-1} recorded on the inclusions can be due merely to the absorption of infrared radiation by ferropericlase-magnesiowustite and, consequently, the presence of carbonates in the inner part of the inclusions cannot be ruled out.

Raman and FTIR analyses carried out on the very low X-ray absorption area at the bottleneck of inclusion 5 did not reveal any feature that could be ascribed to a low-density phase or gas.

DISCUSSION

The mineralogical associations within the studied inclusions, characterized by an abundance of Fe-rich oxides and the presence of carbonates, indicate that the diamond grew in a carbonate-rich environment. This is in line with previously proposed scenarios for formation of ferropericlase–magnesiowüstite-bearing diamonds in carbonate-rich systems (e.g., Kaminsky, 2017 and references therein) and is consistent with the conclusion that the studied inclusions reflect the local diamond-forming environment rather than the ambient deep mantle mineralogy (Nimis et al., 2019). In this light, the composite assemblage found on the flask-shaped inclusion 5 represents the most novel and important finding of this study. The 3D µ-CXRT reconstruction related to µ-Raman mapping show that this inclusion is made of volumetrically dominant magnesiowüstite, which shows evidence of corrosion and partial replacement by an intergrowth of oxides containing oxidized iron, such as hematite–magnetite. Use of a very low laser power ensures that the Fe^{3+}-oxides are natural and are not formed under the incident laser light. Additional detected minor phases include post-spinel polymorphs and an Mg-rich carbonate.

Post-spinel polymorphs of chromite (xieite) and magnesioferrite (maohokite) were previously found in impact craters of meteorites (Chen et al. 2003, 2008; 2019). Laboratory experiments revealed that the spinel/post-spinel transitions for endmember magnesioferrite, magnetite and chromite occur at 20–25 GPa (Mao and Bell 1975; Andrault and Bolfan-Casanova 2001), 23.6 GPa (Fei et al. 1999), and at ≥ 18 GPa and ≥ 1300°C (Ishii et al., 2014), respectively. These data suggest that the high-pressure polymorphs can be stable at Transition Zone to Lower Mantle conditions, as recently confirmed by the discovery of Mg-xieite in Lower-Mantle xenoliths and of nanometric Mn-xieite associated with Fe and Si carbides in super-deep diamonds from Rio Soriso (Juina) (Kaminsky et al. 2015; Kaminsky and Wirth, 2017). Maohokite has not been found in mantle xenoliths nor as inclusion in diamonds. In our case, the position of the main Raman peak of maohokite is the closest to the strong Raman band found at 600 cm^{-1}. This finding represents the first report of post-spinel polymorph of magnesioferrite in diamond. In any case, the presence of a high-pressure polymorph of spinel in inclusion 5 suggests a minimum formation depth within the Transition Zone. Conversely, the presence of huntite (stable to about 6.5 GPa and ca 1000°C; Liu and Lin, 1995) and hematite (stable between 8 and 10 GPa at about 1000 °C) indicate much lower pressure conditions (see Thiele et al. 2017).

The results obtained on our remarkable multiphase inclusion 5 show some apparent inconsistencies that need to be explained: a) the coexistence of high-pressure phases (maohokite and magnesiowustite) with relatively low-pressure phases (huntite, magnetite and hematite); b) the occurrence of hematite, which is stable at higher fO_2 than the host diamond. Although hematite in diamond is commonly considered as an epigenetic inclusion (SilverstmitVekemans et al., 2011), in our case the µ-CXRT results exclude the presence of fractures or cracks connecting inclusion 5 to the surface of the diamond. Moreover, the homogeneity of density around the inclusion, deduced by the X-Ray absorption, indicates that possible healed fractures, if any, could only be filled by diamond and should thus have been closed up during the growth of the diamond. In the absence of evidence for contamination of inclusion 5 after the diamond formation, we cannot consider this inclusion as epigenetic, but its origin is much more complex.

We envisage two possible explanations for the coexistence of high- and low-pressure phases (maohokite and magnesiowüstite vs. huntite, magnetite and hematite) within the same inclusion: 1) solid-state polybaric transformations within the inclusion during the ascent of diamond; or 2) partial reaction of former inclusions with entrapped oxidizing melt at lower pressure. In principle, hematite can form due to decomposition of high-pressure, high-temperature phases during upwelling; for example, at ~10 GPa and 700–1400 °C, magnetite ($FeFe_2O_4$) breaks down to $Fe_4O_5+Fe_2O_3$ (Woodland et al. 2012). Similarly, at about 8-10 GPa and 900-1200°C, magnesioferrite breaks down to Fe_2O_3+MgO (Thiele et al., 2017). If this was the case, however, an analogous reaction forming hematite should have taken place also in the other inclusions 1, 2, and 3, which, instead, contain only small-volume of magnetite/magnesioferrite associated with ferropericlase–magnesiowüstite. The fact that hematite associated with magnetite characterizes only the multiphase inclusion number 5 suggests that the origin of this association cannot be merely related to close-system breakdown of ferropericlase–magnesiowüstite inclusions under changing pressure and temperature during the ascent of diamond.

The aforementioned considerations, as well as the location of inclusion 5 right after a sudden drop in N and H concentrations in the diamond, suggesting an episode of partial diamond resorption, allow reconstruction of the following evolutionary stages:

1. Early growth of diamond and relatively Fe-rich ferropericlase–magnesiowüstite in a carbonate-rich environment led to incorporation of syngenetic ferropericlase–magnesiowüstite inclusions (Nimis et al., 2019) with traces of carbonate. This growth stage was characterized by progressively decreasing concentrations of N (and H) (Agrosì et al., 2017a). Based on the presence of traces of post-spinel high-pressure phases in inclusion 5, this stage took place at depth at least within the Transition Zone.

2. After incorporation of the ferropericlase–magnesiowüstite inclusions, the diamond underwent partial resorption by interaction with hotter or more oxidizing fluids/melts. Resorption was more extensive near the outer inclusion 5 and cut the earlier N zonation. During this reaction stage, the magnesiowüstite of inclusion 5 was exposed to and, possibly, corroded by the circulating fluid/melt. Selective corrosion (Tempesta et al., 2011) on the inner walls of the diamond cavity of inclusion 5 modified its morphology to a rounded subtriangular-flask shape (negative crystal).

3. Advection of a different fluid/melt or a temperature drop allowed the diamond to restart to grow and seal up the cavity hosting the exposed magnesiowüstite inclusion 5. A fraction of the new diamond parent fluid/melt remained trapped around the same inclusion. Thus, part of the content of inclusion 5 can be considered as syngenetic with respect to this growth stage.

4. During the ascent of the diamond, under decreasing temperature and pressure, the entrapped fluid/melt reacted with the magnesiowüstite, causing dismembering of the original inclusion 5 and its partial replacement by Fe^{3+}-rich oxides. The intergrowth of magnetite and hematite that is now observed could be the product of exsolution of a former higher-pressure Fe^{3+}-rich iron oxide (Thiele et al., 2017). Depressurization could be favoured by the high thermal expansion of the entrapped fluid/melt and caused formation of small-volume vacuum/gas in the bottleneck of the inclusion. This hypothesis would also explain the absence of the dark halo and decompression cracks only around this inclusion.

We interpret the composition of the inclusions as further evidence of ferropericlase-bearing diamond formation in a carbonate-rich environment, probably under evolving redox conditions. In particular, the inclusion 5 could be considered as a "snapshot" testifying mixing, redox-freezing and corrosion processes. Although, Kaminsky et al. (2016) suggest a probable origin of the carbonatitic melt within the Lower Mantle, our finding of carbonate-rich melt and of a post-spinel polymorph stable at pressures greater than at least 18 GPa are consistent with Thomson et al. (2016) scenario of diamond formation by redox freezing of slab-derived carbonate melts in the Transition Zone.

Uncited reference

Agrosì et al., 2013, Agrosì et al., 2016, Kaminsky et al., 2013, Kaminsky, 2017, Liu and Lin, 1995, Tempesta and Agrosì, 2016.

Acknowledgements

Appendix A. Supplementary data

⬇ **Download all** supplementary files   Help

The following is the Supplementary data to this article:

📄 Download : **Download XML file (329B)**

Recommended articles   Citing articles (0)

Research data for this article

🔒 *Data not available / Data will be made available on request*

ⓘ About research data ↗

REFERENCES

Agrosì et al., 2013 G. Agrosì, G. Tempesta, E. Scandale, J.W. Harris
    Growth and post-growth defects in a diamond from Finsch mine (South Africa)
    European Journal of Mineralogy, 25 (2013), pp. 551-559
    CrossRef   View Record in Scopus   Google Scholar

Agrosì et al., 2016 G. Agrosì, F. Nestola, G. Tempesta, M. Bruno, E. Scandale, J.W. Harris
    X-ray topographic study of a diamond from Udachnaya: Implications for the genetic nature of inclusions
    Lithos, 248 (25) (2016), pp. 153-159
    Article   📄 Download PDF   View Record in Scopus   Google Scholar

Agrosì et al., 2017a G. Agrosì, G. Tempesta, G.C. Della Ventura, GuidiM.A. Cestelli, M.T. Hutchison, P. Nimis, F. Nestola

Non-destructive in situ study of plastic deformations in diamonds: X-ray Diffraction Topography and µFTIR mapping of two super deep diamond crystals from São Luiz (Juina, Brazil)
Crystals, 7 (Diamond) (2017), p. 233, 10.3390/cryst7080233
CrossRef   Google Scholar

Agrosì et al., 2017b G. Agrosì, G. Tempesta, D. Mele, I. Allegretta, R. Terzano, S.B. Shirey, G. Pearson, F. Nestola
Non-destructive, multi-method, internal analysis of multiple inclusions in a single diamond: First occurrence of mackinawite $(Fe,Ni)_{1+x}S$
American Mineralogist, 102 (2017), pp. 2235-2243
CrossRef   View Record in Scopus   Google Scholar

Andrault and Bolfan-Casanova, 2001 D. Andrault, N. Bolfan-Casanova
High-pressure phase transformations in the MgFe2O4 and Fe2O3-MgSiO3 systems
Physics and Chemistry of Minerals, 28 (2001), pp. 211-217
View Record in Scopus   Google Scholar

Antic et al., 2010 B. Antic, N. Jovic, M.B. Pavlovic, A. Kremenovic, D. Manojlović, M. Vucinic-Vasic, A.S. Nikolić
Magnetization enhancement in nanostructured random type MgFe2O4spinel prepared by soft mechanochemical route
Journal of Applied Physics, 107 (2010), Article 043525, 10.1063/1.3319563
CrossRef   Google Scholar

Chen et al., 2008 M. Chen, J.F. Shu, H. Mao
Xieite, a new mineral of high-pressure $FeCr_2O_4$ polymorph
Chinese Science Bulletin, 53 (21) (2008), pp. 3341-3345, 10.1007/s11434-008-0407-1
CrossRef   View Record in Scopus   Google Scholar

Chen et al., 2003 M. Chen, J. Shu, X. Xie
Natural CaTi2O4-structured FeCr2O4 polymorph in the Suizhou meteorite and its significance in mantle mineralogy. Geochimica and
Cosmochimica Acta, 7 (2003), pp. 3937-3942
Article   Download PDF   View Record in Scopus   Google Scholar

Chen et al., 2019 M. Chen, J. Shu, X. Xie, D. Tan
Maohokite, a post-spinel polymorph of MgFe2O4 in shocked gneiss from the Xiuyan crater in China
Meteoritics & Planetary Science, 54 (3) (2019), pp. 495-502
CrossRef   View Record in Scopus   Google Scholar

Ciucci et al., 1999 A. Ciucci, V. Palleschi, S. Rastelli, A. Salvetti, D.P. Singh, E. Tognoni
CF-LIPS: A new approach to LIPS spectra 37 analysis
Laser part. beams, 17 (1999), pp. 793-797
CrossRef   View Record in Scopus   Google Scholar

D'Ippolito et al., 2015 V. D'Ippolito, G.B. Andreozzi, D. Bersani, P.P. Lottici
Raman fingerprint of chromate, aluminate and ferrite spinels
Journal of Raman Spectroscopy, 46 (2015), pp. 1255-1264, 10.1002/jrs.4764
CrossRef   View Record in Scopus   Google Scholar

de Faria et al., 1997 D.L.A. de Faria, Silva S. Venancio, M.T. de Oliveira
Raman Microspectroscopy of Some Iron Oxides and Oxyhydroxides
Journal of Raman Spectroscopy, 28 (1997), pp. 873-878
View Record in Scopus   Google Scholar

Della Ventura et al., 2014 Della Ventura, G., Marcelli, A., Bellatreccia, F., 2014. SR-FTIR Microscopy and FTIR Imaging in the Earth Sciences. In Reviews in Mineralogy & Geochemistry 78, 447 –480 .
Google Scholar

Fei et al., 1999 Y. Fei, D.J. Frost, H.K. Mao, C.T. Prewitt, D. Hausermann
In situ structure determination of the high-pressure phase of Fe3O4
American Mineralogist, 84 (1999), pp. 203-206
View Record in Scopus   Google Scholar

Harte et al., 1999 Harte, B., Harris, J.W., Hutchison, M.T., Watt, G.R. and Wilding, M.C. (1999) Lower mantle mineral associations in diamonds from Sao Luiz, Brazil. in: Mantle Petrology: Field Observations and High Pressure

Experimentation; a tribute to Francis R. (Joe) Boyd (Y. Fei, C.M. Bertka and B.O. Mysen, editors). The Geochemical Society Special Publication No 6, 125–153.

Google Scholar

Ishii et al., 2014   T. Ishii, H. Kojitani, S. Tsukamoto, K. Fujino, D. Mori, Y. Inaguma, N. Tsujino, T. Yoshino, D. Yamazaki, Y. Higo, K. Funakoshi, M. Akaogi

High-pressure phase transitions in FeCr2O4 and structure analysis of new post-spinel FeCr2O4 and Fe2Cr2O5 phases with meteoritical and petrological implications

American Mineralogist, 99 (2014), pp. 1788-1797, 10.2138/am.2014.4736

CrossRef   View Record in Scopus   Google Scholar

Kaminsky et al., 2013   F. Kaminsky, R. Wirth, A. Schreiber

Carbonatitic inclusions in deep mantle diamond from Juina, Brazil: new minerals in the carbonate-halide association

The Canadian Mineralogist, 51 (5) (2013), pp. 669-688, 10.3749/canmin.51.5.669

CrossRef   View Record in Scopus   Google Scholar

Kaminsky et al., 2016   F.V. Kaminsky, I.D. Ryabchikov, R. Wirth

A primary natrocarbonatitic association in the Deep Earth

Mineralogy and Petrology, 110 (2016), pp. 387-398, 10.1007/s00710-015-0368-4

CrossRef   View Record in Scopus   Google Scholar

Kaminsky and Wirth, 2017   F. Kaminsky, R. Wirth

Nitrides and carbonitrides from the lowermost mantle and their importance in the search for Earth's "lost" nitrogen

American Mineralogist, 102 (2017), pp. 1667-1676

CrossRef   View Record in Scopus   Google Scholar

Kaminsky, 2017   Kaminsky, F. 2017. The Earth's Lower Mantle. Composition and Structure. (ed. Springer) DOI: 10.1007/978-3-319-55684-0.

Google Scholar

Kaminsky et al., 2015   F.V. Kaminsky, R. Wirth, A. Schreiber

A microinclusion of lower-mantle rock and other minerals and nitrogen lower-mantle inclusions in a diamond

The Canadian Mineralogist, 53 (1) (2015), pp. 83-104

CrossRef   View Record in Scopus   Google Scholar

Kiseeva et al., 2018   E.S. Kiseeva, D.M. Vasiukov, B.J. Wood, C. McCammon, T. Stachel, M. Bykov, E. Bykova, A. Chumakov, V. Cerantola, J.W. Harris, L. Dubrovinsky

Oxidized iron in garnets from the mantle transition zone

Nature Geoscience, 11 (2018), pp. 144-147, 10.1038/s41561-017-0055-7

CrossRef   View Record in Scopus   Google Scholar

Liu and Lin, 1995   L. Liu, C.C. Lin

High-pressure phase transformations of carbonates in the system CaOMgOSiO2CO2

Earth and Planetary Science Letters, 134 (3–4) (1995), pp. 297-305

Article   🗋 Download PDF   View Record in Scopus   Google Scholar

Mao and Bell, 1975   Mao H. K. and Bell P. M., 1975. High-pressure transformation in magnesioferrite (MgFe2O4). In: Carnegie Institution of Washington Year Book 75, 555–557.

Google Scholar

McCammon et al., 1997   C. McCammon, M. Hutchison, J. Harris

Ferric Iron Content of Mineral Inclusions in Diamonds from São Luiz: A View into the Lower Mantle

Science, 278 (5337) (1997), pp. 434-436, 10.1126/science.278.5337.434

View Record in Scopus   Google Scholar

Nestola et al., 2018   F. Nestola, N. Korolev, M. Kopylova, N. Rotiroti, G. Pearson, M.G. Pamato, M. Alvaro, L. Peruzzo, J.J. Gurney, A.E. Moore, J. Davidson

CaSiO3 perovskite in diamond indicates the recycling of oceanic crust into the lower mantle

Nature, 555 (7695) (2018), pp. 237-241, 10.1038/nature25972

2018

CrossRef   View Record in Scopus   Google Scholar

Nimis et al., 2019

P. Nimis, F. Nestola, M. Schiazza, R. Reali, G. Agrosì, D. Mele, G. Tempesta, D. Howell, M.T. Hutchison, R. Spiess

Fe-rich ferropericlase and magnesiowüstite inclusions reflecting diamond formation rather than ambient mantle

Geology, 47 (1) (2019), pp. 27-30, 10.1130/G45235.1

CrossRef   View Record in Scopus   Google Scholar

Pal'yanov et al., 2013 Y.N. Pal'yanov, Y.V. Bataleva, A.G. Sokol, Y.M. Borzdov, I.N. Kupriyanov, V.N. Reutsky, N.V. Sobolev

Mantle–slab interaction and redox mechanism of diamond formation

PNAS (2013), 10.1073/pnas.1313340110

201313340

Google Scholar

Palot et al., 2016 M. Palot, S.D. Jacobsen, J.P. Townsend, F. Nestola, K. Marquardt, N. Miyajima, J.W. Harris, T. Stachel, A. McCammonC, G. Pearson

Lithos, 265 (2016), pp. 237-243

Article   📄 Download PDF   View Record in Scopus

SilverstmitVekemans et al., 2011 G. Silverstmit, B. Vekemans, K. Appel, S. Schmitz, T. Schoonjans, F.E. Brenker, F. Kaminsky, L. Vincze

Three-Dimensional Fe Speciation of an Inclusion Cloud within an Ultradeep Diamond by Confocal μ-X-ray Absorption Near Edge Structure: Evidence for Late Stage Overprint

Analytical. Chemistry, 83 (2011), pp. 6294-6299 dx

10.1021/ac201073s

Google Scholar

Smith et al., 2016 E.M. Smith, S.B. Shirey, F. Nestola, E.S. Bullock, J. Wang, S.H. Richardson, W. Wang

Large gem diamonds from metallic liquid in Earth's deep mantle

Science, 354 (2016), pp. 1403-1405

https://doi.org/10.1126/science.aal1303

CrossRef   View Record in Scopus   Google Scholar

Smith et al., 2018 E.M. Smith, S.B. Shirey, S.H. Richardson, F. Nestola, E. Bullock, J. Wang, W. Wang

Blue boron-bearing diamonds from Earth's lower mantle

Nature, 560 (2018), pp. 84-87, 10.1038/s41586-018-0334-5

CrossRef   View Record in Scopus   Google Scholar

Tempesta and Agrosì, 2016 G. Tempesta, G. Agrosì

Standardless, minimally destructive chemical analysis of red beryls by means of Laser Induced Breakdown Spectroscopy

European Journal of Mineralogy, 28 (2016), pp. 571-580, 10.1127/ejm/2016/0028-2529

CrossRef   View Record in Scopus   Google Scholar

Tempesta et al., 2011 G. Tempesta, E. Scandale, G. Agrosì

Striations and hollow channels in rounded beryl crystals

Periodico di Mineralogia, 79/1 (2011), pp. 75-87

View Record in Scopus   Google Scholar

Thiele et al., 2017 L.U. Thiele, A.B. Woodland, T. Boffa Ballaran, N. Miyajima, D.J. Frost

Phase relations of MgFe2O4 at conditions of the deep upper mantle and transition zone

American Mineralogist, 102 (2017), pp. 632-642

Google Scholar

Thomson et al., 2016 A.R. Thomson, M.J. Walter, S.C. Kohn, R.A. Brooker

Slab melting as a barrier to deep carbon subduction

Nature, 529 (2016), pp. 76-79

CrossRef   View Record in Scopus   Google Scholar

Woodland et al., 2012 A.B. Woodland, D.J. Frost, D.M. Trots, K. Klimm, M. Mezouar

In situ observation of the breakdown of magnetite (Fe_3O_4) to Fe_4O_5 and hematite at high pressures and temperatures

American Mineralogist, 97 (2012), pp. 1808-1811

CrossRef   View Record in Scopus   Google Scholar